Patient-Specific Finite-Element Analyses of the Proximal Femur with Orthotropic Material Properties Validated by Experiments

Nir Trabelsi

Zohar Yosibash
e-mail: zohary@bgu.ac.il

Department of Mechanical Engineering
Ben-Gurion University of the
Negev Beer-Sheva,
84105, Israel

Patient-specific high order finite-element (FE) models of human femurs based on quantitative computer tomography (QCT) with inhomogeneous orthotropic and isotropic material properties are addressed. The point-wise orthotropic properties are determined by a micromechanics (MM) based approach in conjunction with experimental observations at the osteon level, and two methods for determining the material trajectories are proposed (along organs outer surface, or along principal strains). QCT scans on four fresh-frozen human femurs were performed and high-order FE models were generated with either inhomogeneous MM-based orthotropic or empirically determined isotropic properties. In vitro experiments were conducted on the femurs by applying a simple stance position load on their head, recording strains on femurs' surface and head's displacements. After verifying the FE linear elastic analyses that mimic the experimental setting for numerical accuracy, we compared the FE results to the experimental observations to identify the influence of material properties on models' predictions. The strains and displacements computed by FE models having MM-based inhomogeneous orthotropic properties match the FE-results having empirically based isotropic properties well, and both are in close agreement with the experimental results. When only the strains in the femoral neck are being compared a more pronounced difference is noticed between the isotropic and orthotropic FE result. These results lay the foundation for applying more realistic inhomogeneous orthotropic material properties in FEA of femurs. [DOI: 10.1115/1.4004180]

Keywords: Proximal femur, Finite element analysis, p-FEM, Computed tomography (CT), Micromechanics, Anisotropic materials, Bone biomechanics

1 Introduction

Patient-specific finite element (FE) analyses of the human femur are widely used nowadays to predict its mechanical response (see, e.g., Refs. [1–4], and references therein). The validity of the FE results depends largely on an accurate description of bone's geometry and proper assignment of material properties to the FE model [5–8]. The generation of the bone's geometry (and thereafter the FE mesh) is considered, in large extent, as a solved problem [6,8–11]. The proper assignment of material properties on the other hand, is still under active research because of the inherent inhomogeneous and anisotropic nature of bone's tissue (in addition to the homogenization process). Most past FE studies assumed the bone to be inhomogeneous isotropic [1,3,5,7,10,12–14] due to simplicity and the limited knowledge of the anisotropic behavior. Based on the relationship between CT numbers, Hounsfield Units (HU) and a density measure ρ, the inhomogeneous Young's modulus $E[\rho(HU)]$ has been estimated empirically [15,16]. Many empirical $E(\rho)$ relations are reported and their influence on FE-predictions was widely investigated (see, e.g., Ref. [3]). The *isotropic strategy* has also been motivated by limited comparative studies claiming that the assigned orthotropic material model has a minor influence on the FE result compared to the isotropic one. Peng et al., for example, compared FE models in using orthotropic and inhomogeneous isotropic properties (although no experimental data were presented) and concluded that the differences are negligible [13]. Baca et al. compared FE models of the proximal femur and "small" specimens with either isotropic or orthotropic inhomogeneous properties [17]. The reported results show a significant difference for small bone specimens, whereas in the entire organ (proximal femur), the difference is negligible. A recent numerical study [18] concluded that the differences between the two property assignments are more significant (maximum differences in Von Mises stresses about 13%) in some local region. This conclusion is limited since in Ref. [18] only one bone specimen was modeled and no comparison to experiments was conducted.

Although some empirical relations between the orthotropic constants and bone density have been suggested [19–23], the determination of material trajectories from clinical quantitative computed tomography (QCT) scans remains an open question. Several recent preliminary studies have attempted to determine these trajectories on pieces of cortical femurs or vertebra [24,25]. Instead of the empirical HU-elastic property relations, we investigate herein inhomogeneous orthotropic properties derived by a micromechanical (MM) homogenization approach based on the microstructure and vascular porosity as suggested by Fritsch and Hellmich in Ref. [26] in combination with experimental data obtained at the osteon Level [27]. This approach is chosen because the trabecular fabric cannot be determined using clinical CT scans and trabecular bone morphology cannot be determined (see Refs. [28–30] for the use of the fabric tensor in the case of μCT or high-resolution peripheral QCT may be applied). The MM-homogenization approach adopted is aimed at overcoming this limitation. A variation of the method presented herein was proven beneficial

Contributed by the Bioengineering Division of ASME for publication in the Journal of Biomechanical Engineering. Manuscript received November 29, 2010; final manuscript received March 30, 2011; published online xx xx, xxxx. Assoc. Editor: Stephen Klisch.

Table 1 Summary of the fresh-frozen femurs and CT scan resolution

Notation	Age	Gender	Side	Death reason	Slice thickness (mm)	Pixel (mm)
FF1	30	Male	Left	Car accident	0.75	0.78125
FF2	20	Female	Right	Stroke	1.5	0.72851
FF3	54	Female	Left	Cardiovascular disease	1.25	0.51757
FF4	63	Male	Right	Car accident	1.25	0.19531

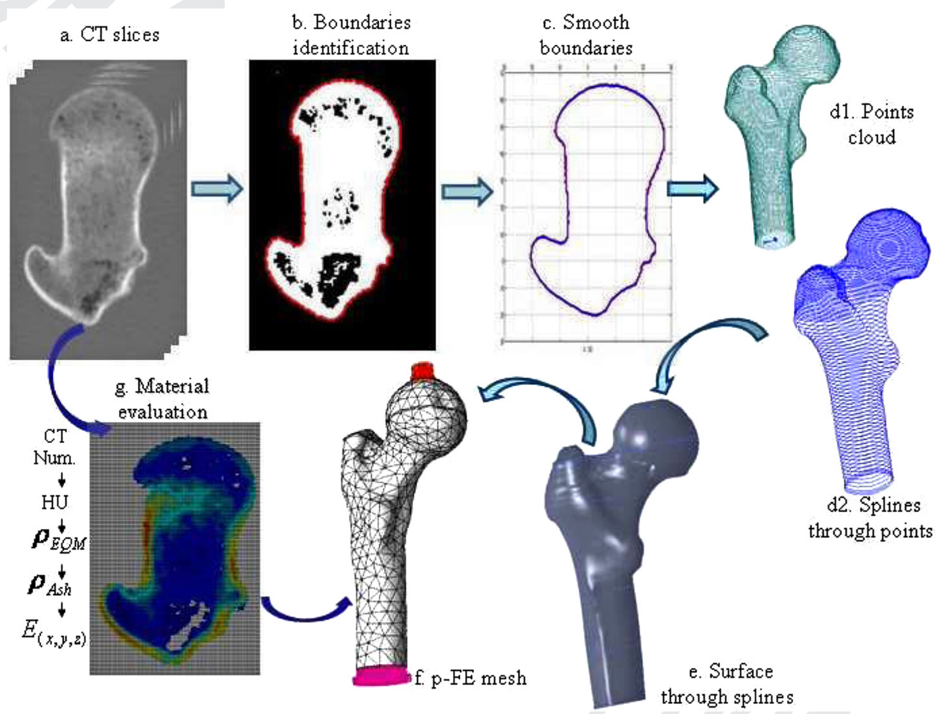

Fig. 1 Schematic flow chart describing the generation of the p-FE model from QCT scans: (*a*) typical CT-slice, (*b*) contour identification, (*c*) smoothing boundary points, (*d*1) points cloud representing the bone surface, (*d*2) close splines for all slices, (*e*) bone surface, (*f*) p-FE mesh, and (*g*) material evaluation from CT data

in the case of a human mandible simulation [31] and in Ref. [32] it was used to generate a FE model of the femur with *inhomogeneous isotropic* material properties, considering for the first time an inhomogeneous Poisson ratio. Herein we extend the MM approach by assigning inhomogeneous orthotropic material properties to high-order FE models using QCT preformed on four femurs. In addition to determining the "bone matrix" material tensor from experimental observations, we also investigate two methods for determining material trajectories: (a) following the contour of femur's outer surface and (b) along the principal strain directions. The FE results are compared to these obtained with isotropic material and to the experimental observations on four different fresh frozen femurs.

2 Methods

Four fresh-frozen human femurs were CT scanned, followed by in vitro mechanical experiments. The QCT scans were manipulated to generate patient-specific high-order FE bone models that mimic the experimental conditions. The semiautomatic 3D reconstruction of the femur's geometry and generation of FE-meshes are detailed in Refs. [3,4,10] and briefly summarized herein. All DICoM (Digital Imaging and Communication in Medicine) format QCT scans were automatically manipulated by in-house computer codes. First the scans are transformed into binary images in which nonzero pixels belong to the femur domain and 0-value is assigned to pixels associated with the background (scan resolutions are summarized in Table 1). Exterior, interface (between trabecular and cortical bone), and interior boundaries are traced in each slice and the points on these boundaries are manipulated by a 3D smoothing algorithm to generate "smooth boundary representation." The same boundaries are used to determine the cortical, trabecular, and cavity regions within the femur. An auto-mesher is thereafter applied within the p-FE code StressCheck that generates tetrahedral high-order elements.[1] The entire algorithm (QCT to FE) is schematically illustrated in Fig. 1.

The polynomial degree over the elements was increased until convergence in energy norm and strains at the points of interest was observed. Each FE model consists between 3500 to 4500 elements [$\sim 150{,}000$ degrees of freedom (DOFs) at $p=4$ and $\sim 300{,}000$ DOFs at $p=5$]. The proper material properties are directly extracted from the QCT scanned and assigned to each integration point (512 points for each tetrahedral element) (details are provided in Sec. 2.1). For an orthotropic material the material directions are also determined (as explained in Sec. 2.1.3). Clamped boundary conditions are assigned to the distal part and traction is applied on the head to mimic the experimental conditions. The surface of the femur is accurately represented in the FE model by using the blending function method [33]. In the *p*-

[1]StressCheck is trademark of Engineering Software Research and Development, Inc, St. Louis, MO, USA.

PROOF COPY [BIO-10-1416] 006105JBY

version of the FE method convergence is realized by keeping a fixed mesh (with relatively large elements) and increasing the polynomial degree of the approximated solution. Therefore, the accurate geometrical description of the domain must be realized which is being accomplished by the use of blending-function mapping.

2.1 Material Properties Assignment. Inhomogeneous orthotropic properties derived based on the micromechanics analysis are assigned to the FE models representing the femurs. Herein we compare the mechanical response predicted by these models to FE models having isotropic material properties determined empirically.

2.1.1 Isotropic Material Properties Determined by Empirical Correlation. Many empirical relations between Young's modulus and bone density, with a constant Poisson's ratio are available, see, e.g., Refs. [34–38]. In Refs. [3,4] we found that *p*-FE analyses with the Keyak relationship [36] provide the closest results to in vitro experiments on the proximal femur:

$$\rho_{\mathrm{EQM}} = 10^{-3}(a \times HU - b)\left(\mathrm{g/cm^3}\right) \tag{1}$$

$$\rho_{\mathrm{Ash}} = \left(1.22 \times \rho_{\mathrm{EQM}} + 0.0523\right)\left(\mathrm{g/cm^3}\right) \tag{2}$$

$$E_{\mathrm{Cort}} = 10200 \times \rho_{\mathrm{Ash}}^{2.01}\ (\mathrm{MPa}) \tag{3}$$

$$E_{\mathrm{Trab}} = 5307 \times \rho_{\mathrm{Ash}} + 469\ (\mathrm{MPa}) \tag{4}$$

where ρ_{EQM} is the equivalent mineral density; ρ_{Ash} is the ash density; $E_{\mathrm{Cort}}, E_{\mathrm{Trab}}$ are the Young's moduli in the cortical and trabecular regions and the parameters a and b are determined by the K_2HPO_4 phantoms in the CT-scan. Poisson's ratio is constant $\nu = 0.3$.

2.1.2 MM-based Orthotropic Material Properties. A continuum MM-based model (details are available in Refs. [31,32] is applied on the QCT scans to determine (nonempirical) relations between orthotropic elasticity tensor components and HU. It is based on two consecutive steps [26,31]:

- Based on voxel average rules for the attenuation coefficients, we assign to each voxel the volume fraction occupied by water (marrow) and that occupied by solid bone matrix. The volume fraction is identical to the vascular porosity, as given by

$$\phi(x) = \begin{cases} \frac{HU_{\mathrm{BM}} - HU(x)}{HU_{\mathrm{BM}}} & \forall\ HU \le 1600 \\ 0 & \text{otherwise} \end{cases} \tag{5}$$

  We denote by x the position of the individual voxel with $HU = 0$ representing pure water, and $HU_{\mathrm{BM}} \ge 1600$ represents a "perfectly compact" bone in a human femur (see Ref. [32] for details). The lower HU values refer to very porous trabecular bone, with a vascular porosity (ϕ) close to 100%. At the upper end of the HU, values are identified as associated with vanishing vascular porosity $\phi \sim 0$.
- By means of a MM model for bone based on mechanical properties of solid bone matrix and of water, we convert ϕ into voxel-specific orthotropic material tensor components. The model, cast in the framework of random homogenization theory [31], is of the Mori–Tanaka type, so that the effective stiffness tensor $\mathbb{C}_{\mathrm{eff}}$ of the bone at position x is given by

$$\mathbb{C}_{\mathrm{eff}} = \{\phi\mathbb{C}_{H_2O} : [\mathbb{I} + \mathbb{P}_{\mathrm{cyl}} : (\mathbb{C}_{H_2O} - \mathbb{C}_{\mathrm{BM}})]^{-1} + (1-\phi)\mathbb{C}_{\mathrm{BM}}\} : \\ : \{\phi[\mathbb{I} + \mathbb{P}_{\mathrm{cyl}} : (\mathbb{C}_{H_2O} - \mathbb{C}_{\mathrm{BM}})]^{-1} + (1-\phi)\mathbb{I}\}^{-1} \tag{6}$$

  where $\mathbb{I}$ is the fourth-order identity tensor (A3), $\mathbb{P}_{\mathrm{cyl}}$ is the fourth-order Hill tensor (A4) accounting for the cylindrical pore shape in a bone matrix of stiffness $\mathbb{C}_{\mathrm{BM}}$ (A1), $\mathbb{C}_{H_2O}$ (A2) is the bulk elastic stiffness and colons denote the second-order tensor contraction (see further details in Appendix A).

The bone-matrix material tensor can be obtained at the microlevel by either ultrasonic [40] or nanoindentation techniques [27]. The identification of orthotropic constant for bone is still an open problem therefore six relevant studies are presented in Table 4 in Appendix A to provide an overview of the available knowledge and to demonstrate the material properties range. A preliminary investigation was undertaken by which the properties in Refs. [40] and [27] were applied in the MM model:

$$\mathbb{C}_{\mathrm{BM}}^{[1]} = \begin{pmatrix} 18.5 & 10.3 & 10.4 & 0 & 0 & 0 \\ 10.3 & 20.8 & 11.0 & 0 & 0 & 0 \\ 10.4 & 11.0 & 28.4 & 0 & 0 & 0 \\ 0 & 0 & 0 & 12.9 & 0 & 0 \\ 0 & 0 & 0 & 0 & 11.5 & 0 \\ 0 & 0 & 0 & 0 & 0 & 9.3 \end{pmatrix} (\mathrm{GPa}),$$

$$\mathbb{C}_{\mathrm{BM}}^{[11]} = \begin{pmatrix} 20.8 & 10.4 & 16.6 & 0 & 0 & 0 \\ 10.4 & 22.1 & 16.5 & 0 & 0 & 0 \\ 16.6 & 16.5 & 41.9 & 0 & 0 & 0 \\ 0 & 0 & 0 & 15.4 & 0 & 0 \\ 0 & 0 & 0 & 0 & 11.2 & 0 \\ 0 & 0 & 0 & 0 & 0 & 9.4 \end{pmatrix} (\mathrm{GPa}) \tag{7}$$

The resulting inhomogeneous orthotropic material properties were assigned on our FE models. Those studies were chosen since they both reported on all required material constant, they used different experimental tool and they represent well the range of the reported material properties. Our models shows that $\mathbb{C}_{\mathrm{BM}}^{[1]}$ results in a "weak" response compared to several experimental results [40]. Based on our preliminary results the current study adopts the elastic constant suggested in Ref. [27] to be used in the MM model in conjunction with the *p*-FE model.

2.1.3 Determination of Material Trajectories. For an orthotropic material the material trajectories at each point have to be determined. The (vectorial) material trajectories cannot be determined clearly from a clinical CT scan thus additional information like the characteristic density distributions within the bony organ or the organ's surface description may be used [26,41]. Herein, we tested two alternative assumptions to obtain the inhomogeneous (voxel-specific) material trajectories: (a) either following the femur's outer geometry (determined by the biological evolution of the bone to best carry the loading) or (b) following the principal strains (see, e.g., Ref. [42]). In both cases, we consider the longitudinal direction (axis-3) as the "stiff" material direction (having the largest Young's modulus) and the other two transverse directions as weak (having the smaller Young's modulus). The transverse plane is rather isotropic (E_1 is close in value to E_2). In this section we outline the algorithms for determining the normal vectors that represent material trajectories.

2.1.3.1 Material trajectories according to outer surface geometry. By assuming that material trajectories follow the outer surface, we developed a three-step algorithm to determine these:

a) Creation of smooth boundary surfaces from CT data: CT data is processed as shown in Figs. 1(*b*), 1(*c*), and 1(*d1*): Bone borders are detected at each CT slice, then a 3D smoothing algorithm is applied and finally a cloud of point is kept that represent femur's boundary used for surface reconstruction.
b) Computation of the closest point (CP) on femurs outer surface: For each point of interest (POI) at which trajectories are sought, the closest point (CP) on the outer surface

ID: sambasivamt Time: 04:45 I Path: Q:/3b2/JBY#/Vol00000/110002/APPFile/AI-JBY#110002

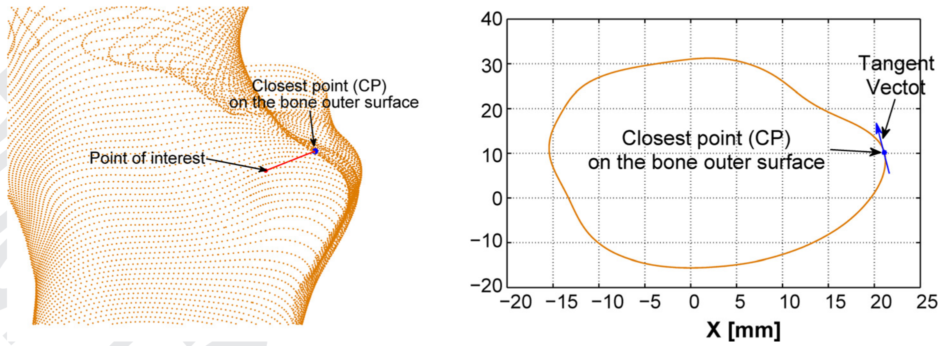

Fig. 2 Left closest point (CP) on the bone outer surface to a specific POI. Right: tangent (circumferential) direction.

is identified, by minimizing the distance among all points on the surface:

$$R = \min_{x\,\text{on surface}} \times \left[\sqrt{(x_{\text{surface}} - x_{\text{POI}})^2 + (y_{\text{surface}} - y_{\text{POI}})^2 + (z_{\text{surface}} - z_{\text{POI}})^2}\right] \qquad (8)$$

see Fig. 2, left. The material trajectories related to the CP are then assigned to the POI.

c) Computing radial, circumferential (tangent), and longitudinal trajectories: The circumferential (tangent) direction is the vector that follows the direction of a spline at the CP, see Fig. 2, right. The longitudinal direction is the one parallel to the bone surface and associated to the gradient along the z axis. The closest points to the CP on the spline below and above the spline on which the CP is located are found. The vector connecting these two points is the longitudinal direction. The radial (normal) direction is easily computed by the vector product of the longitudinal and tangent vectors. The three normalized direction vectors form the material trajectories at the POI.

2.1.3.2 Material trajectories following principal strains. Another possibility to determine material trajectories is motivated by Wolff's law [43], and associated with strains principal directions. The main assumption is that bone tissue orientation correlates well to principal strain direction [44]. The stance position loading (the magnitude of load does not influence the principal directions but only the magnitude of the strains) is used for approximating the principal strain directions assuming a homogeneous isotropic material. This approach is also motivated by the recent experimental results in Ref. [45], which show that the principal strain directions on the femur's surface is almost independent on the loading conditions on the femur's head, covering the range of directions spanned by the hip joint force. Although the principal strains magnitude varied greatly between loading configurations, the principal strain direction varied very little. This suggests that the anatomy and the distribution of anisotropic material properties in the proximal femur is probably not strongly affected by the various loading directions, and can be determined from the direction of the principal strains resulting from the stance loading configuration.

At each POI the principal strains are computed and the "stiffest" direction 3 is associated with the largest absolute value of the strain tensor eigenvalues. For each POI at x, the coordinate system along principal strain directions is denoted by X^m_α, $\alpha = 1, 2, 3$ (3 is the "stiffest"). Since the material tensor $\mathbb{C}^m$ is assumed to be along X^m_α it is transformed into the femur's coordinate system by [46]

$$C_{ijkl} = C^m_{\alpha\beta\gamma\delta}\ell_{\alpha i}\ell_{\beta j}\ell_{\gamma k}\ell_{\delta l} \qquad (9)$$

where $\ell_{\alpha i} \equiv \cos(X^m_\alpha, x_i)$

2.1.4 The "Stiffest" Material Trajectory. We preformed numerical tests to evaluate the differences of obtained trajectories by the two proposed methods. Figure 3 presents the difference in the material trajectories in the "stiffest" on a typical 2-3 plane. Several points of interest are presented to exemplify the specific distribution of the "stiffest" material trajectory.

In most of the shaft region the "stiffest" trajectory is orientated along the femur's x_3 axis and is in agreement with other studies [25]. For POIs close to femur's outer boundary in the head and neck regions, both methods result in similar directions. In the central femoral's head and neck; on the other hand, the directions are different.

The different methods' influence on the FE results was numerically tested. Same MM orthotropic law but with material trajectories based on bone's geometry and the other based on principal strains were applied to the FE models. Strain and displacements on bone surface were compared. No significant differences in the FE result was demonstrated (mean error was less than 5%). Since there is no clear advantage of one method over the other, we determine the material trajectories following the principal strains. The main reasons for this choice are the complexity and long computational times when using the geometric based method compared to the robustness in the principal strains method.

2.2 Mechanical Experiments. In vitro experiments on four fresh-frozen proximal femurs summarized in Table 1 were used to assess the validity of FE simulations.

The experiments simulate a simple stance position configuration in which the femurs were loaded through their head while inclined at two different inclination angles (0° and 20°) as shown in Fig. 4. We measured the vertical and horizontal displacements of femur's head, the strains at the inferior and superior parts of the neck, and on the medial and lateral femoral shaft. Between 5 and 10 strain-gauges were bonded on each of the tested femurs. In all experiments a linear response between force and displacements and strains was observed beyond 200N preload. The experimental error is within a ±5% range. This range was estimated by the measurements error (calibration to known displacements/loads/strains), deviation between consecutive measurements and estimation of the linear response (details are provided in Refs. [4,10].

3 Results

3.1 Comparison of Material Properties. The MM-based orthotropic constants are compared to the empirical isotropic Young's modulus given by Refs. [34,47] in Fig. 5 [empirical shear modulus is computed with $(\nu = 0.3)$]. In the longitudinal direction (E_3) is higher for $HU < 1400$ while in the transverse detections $(E_1$ and $E_2)$ are smaller compared to the isotropic empirical E, whereas the Poisson ratio is clearly nonconstant. Similar shear moduli are obtained for $HU < 600$. One can notices that $(0.9 < E_1/E_2 < 1)$ and $(0.3 < E_2/E_3 < 0.6)$, supporting our

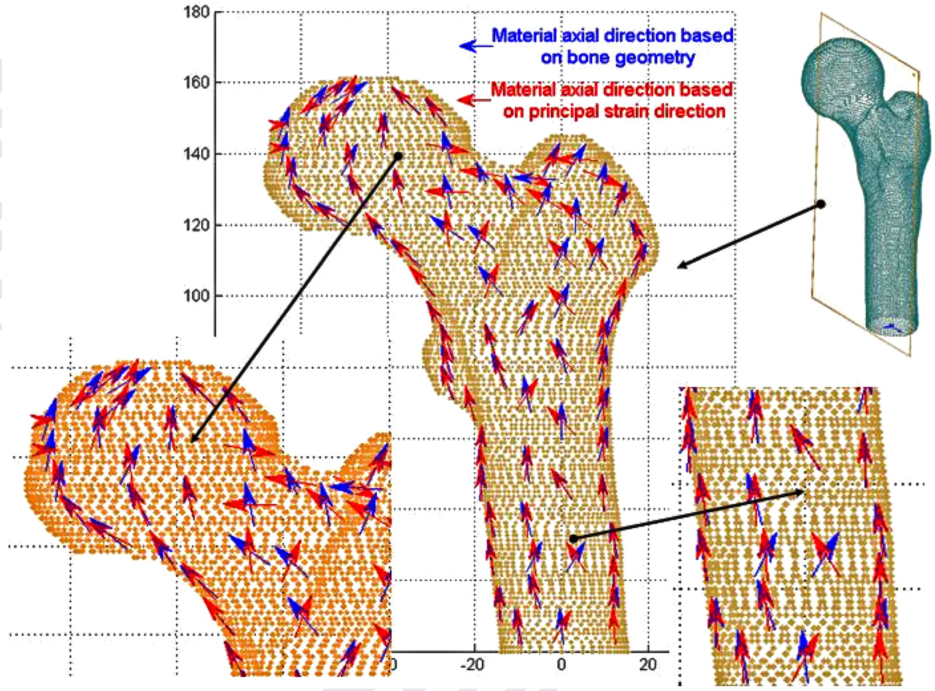

Fig. 3 Axial material trajectories throughout a femur, zoomed portion in the trabecular area and femoral neck (left) and zoomed portion in cortical area and shaft (right)

observation that the longitudinal direction is the "stiff" one and that the transverse direction is rather isotropic.

3.2 FE Results Using Isotropic and Orthotropic Properties Compared to Experimental Observations. We monitor the p-FE convergence in energy norm, obtaining for $p = 4$ an error smaller than 2%. The experimental measured strains on femur's surface at several locations and the vertical and horizontal displacements of the femur's head are used for comparison purposes. At the same locations the strains in the direction of the strain-gauges and displacements were extracted from the FE solutions. The FE strains are reported as the average over a face element on which the strain-gauge is bonded in reality because the strain-gauge (SG) readings are also an averaged value over SG's length. In Fig. 6 we present, for example, these locations on the FE model of FF3. To estimate quantitatively the validity of the various FE models, we compared *all measured data* (both displacements and strains for the four femurs of interest) to the computed data, i.e., we computed the linear regression between the data sets and the normalized root mean squared error (NRMSE). Figure 7 presents a linear regression of the experimental results compared to FE predictions, for both displacements and strains (for a load of 1000*N*). These linear regressions demonstrate the general quality assessment of the analysis. A very good correlation is obtained between the predicted and measured strains and displacements for the empirical based isotropic model. The orthotropic model makes the model "less stiff" but still a good correlation to the experiments is observed. In spite of

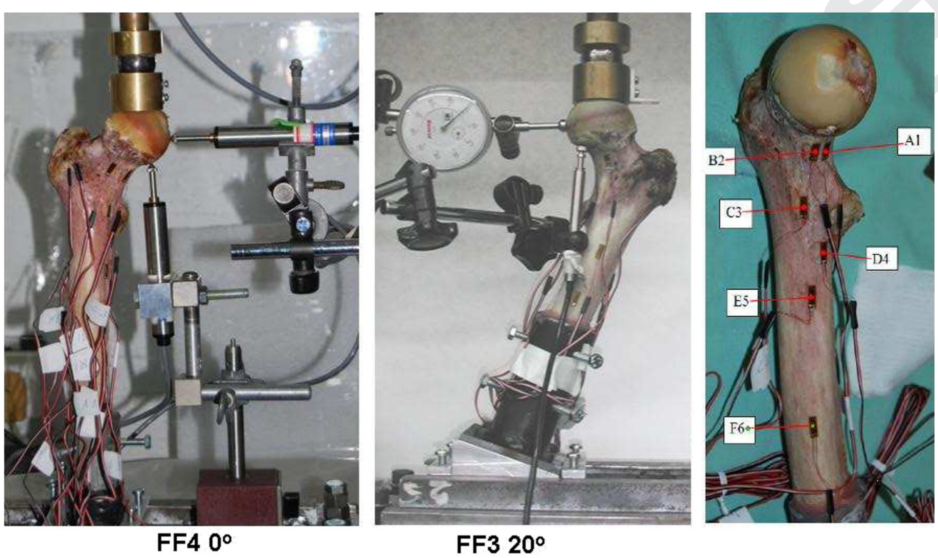

Fig. 4 Typical experiments on fresh-frozen bones (FF3 and FF4) at different inclination angles. Right: Strain gauges location at the neck and shaft regions.

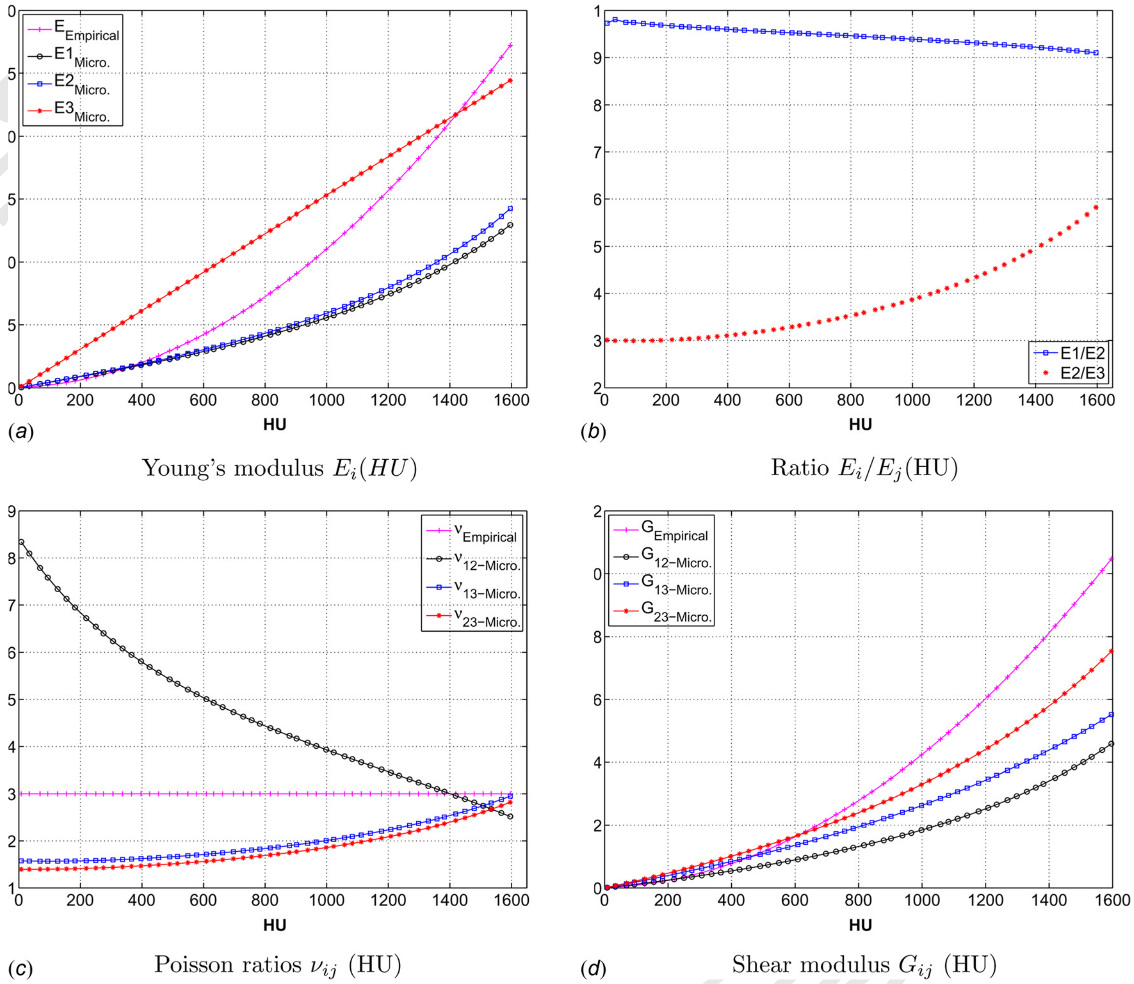

Fig. 5 (*a*) *E*(*HU*) relation for orthotropic MM-based and isotropic empirical-based models [34,47]. (*b*) Ratio of Young's modulus in different directions. (*c*) Poisson ratio dependence on HU for MM-based model ($\nu = 0.3$ for empirically based model). (*d*) Shear moduli relation to HU for MM-based and empirically based models.

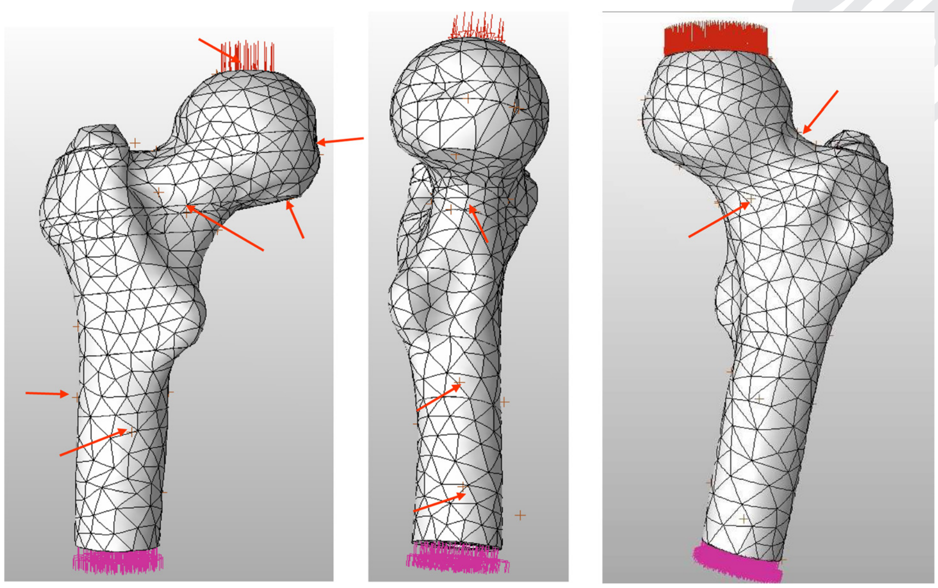

Fig. 6 FF3-FE model and locations at which displacements and strains were computed and measured in the experiment

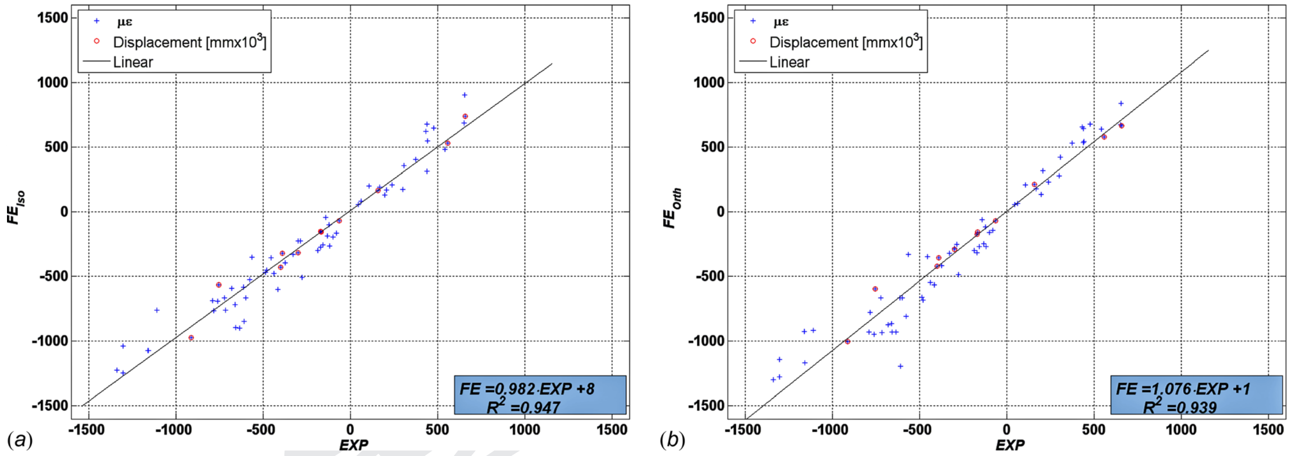

Fig. 7 Comparison of the computed strains + and displacements ⊕ to the experimental observations. Material properties assigned by two different strategies in the FE models: (*a*) empirical-based, (*b*) MM-based.

differences presented in Fig. 7, for biological structures the results are of comparable accuracy (less than 10%).

Since the loading in our experiments implies mostly normal strains and displacements in the longitudinal direction with no shearing or torsion, the close results between isotropic and MM orthotropic based models are very reasonable. To further examine the differences between the two models, we compare separately the results obtained for different inclination angles (0° and 20°). In addition, the results were divided into three main groups of interest: strains at the femur's neck region, strains at the femur's shaft region and displacements of femur's head. A summary of the comparisons is presented in Table 2. To quantify and emphasize the differences between the isotropic versus the orthotropic model, a comparison between the FE results based on the different material models is presented in Table 3.

4 Discussion

It is widely accepted that bone-tissue is orthotropic rather than isotropic, and that the main orientation of bone's microstructure appears to adapt along principal strains [20,42]. Studies comparing the mechanical response under isotropic and very restricted orthotropic material properties under a stance loading condition, conclude that a very similar response is obtained; however, none of these used models that represent realistic local anisotropy throughout the entire bone and no comparison to experimental observation was reported [13,17,18]. Encouraged by promising studies addressing anisotropy in bones [31,32] we developed herein a systematic micromechanics-based algorithm to evaluate inhomogeneous orthotropic bone's properties based on QCT scans. Material parameters obtained by the MM approach are shown to lie within the range of these obtained by empirical methods in various past publications.

Two automatic methods to determine the anisotropic material trajectories were found to be very similar in the shaft and close to bone's surface in the head, but differ in the internal portion of the head. The MM based material properties in femur's head were compared to experimental observations in a recent study by Ohman et al. [48], adding another level of confidence in the proposed MM algorithm. Ohman et al. extracted cylindrical specimens from femoral heads with alignment and misalignment to the trabecular main direction of approximately 20°. The Young's modulus values reported in Ref. [48] were 2.76(±1.06) GPa for the "aligned" and 1.59(±0.66) GPa for the "misaligned" groups, related to $100 < HU < 250$. About 40% difference was found in measured Young's modulus in the 'misaligned' specimens, lower than these in the "aligned" ones. In all femurs investigated herein we found that the Young's modulus is in the same range as reported by Ohman et al. and varies about 30–40% if rotated by 20°, as observed in Ref. [48].

QCT-scans were used to generate isotropic and orthotropic FE models of four fresh-frozen human femurs harvested from both genders and age span of 20–63 years-old. The reliability of the FE results and the influence of the assigned material properties was estimated by comparison to strains and displacements obtained by in vitro experiments. It is important to realize that the mechanical tests represent a very simple loading condition which is not necessary physiological. The simple loading condition is due to experimental constraints and aimed at reducing the complexity of the mechanical response.

Table 2 Summary of linear regression and NRMSE: FE results compared to experimental observations. All results = both strains and displacements, SGs: strain gauge results, NRMSE $= \sqrt{\Sigma_{i=1}^{n}(x_i - y_i)^2/n}/[\max(x) - \min(x)]$.

Region and tilt	Material model	Slope	R^2	NRMSE
All results	iso.	1.01	0.96	0.06
Tilt 0°	orth.	1.09	0.96	0.07
All results	iso.	0.88	0.91	0.08
Tilt 20°	orth.	1.04	0.88	0.10
All results	iso.	0.98	0.95	0.06
Tilt 0°, 20°	orth.	1.08	0.94	0.07
All SGs	iso.	1.02	0.96	0.06
Tilt 0°	orth.	1.10	0.96	0.08
All SGs	iso.	0.87	0.90	0.09
Tilt 20°	orth.	1.03	0.87	0.11
All SGs	iso.	0.98	0.94	0.06
Tilt 0°, 20°	orth.	1.09	0.93	0.08
Displacements	iso.	0.99	0.98	0.04
Tilt 0°, 20°	orth.	1.0	0.99	0.04
Shaft region	iso.	1.1	0.94	0.07
Tilt 0°, 20°	orth.	1.06	0.93	0.08
Neck region	iso.	0.88	0.96	0.06
Tilt 0°, 20°	orth.	1.09	0.94	0.09

Table 3 Linear regression and NRMSE: isotropic versus orthotropic FE results (tilt 0° and 20°)

Region of interest	Slope	R^2	NRMSE
All results	1.08	0.97	0.05
All SGs	1.09	0.97	0.06
Displacements	1.01	0.99	0.02
Shaft region	0.97	0.99	0.02
Neck region	1.24	0.97	0.10

The strains and displacements computed by the *p*-FEMs with inhomogeneous MM-based orthotropic properties in conjunction with material trajectories along principal strains correlate well with the experimental observations. The comparison presented in Table II demonstrates that if the principal strains or head displacements are of interest, the differences between the results of the isotropic empirical based model and the orthotropic MM model are small and in the range of the experimental errors. On the other hand, a more pronounced difference is noticed between the isotropic and orthotropic FE results when only strains in the femoral neck are compared. To assess if the orthotropic and isotropic models yield similar results for a more complex state of loading we applied on the same FE models a compression load on femur's head in addition to a torsional load (resulting in a moment along the *z* axis). Because experiments with complex loading configurations on fresh-frozen human femurs are unavailable at this time, we only address the numerical results. Comparing the FE predicted strains by the different material models show a significant differences between them $(\text{slope} = 1.35, R^2 = 0.96, \text{NRMSE} = 0.14,$ and $\text{slope} = 1.19, R^2 = 0.99, \text{NRMSE} = 0.09$ for displacements). This numerical study demonstrates that when a more complex loading condition is applied, the FE predicted mechanical response of the femur is considerably different (the orthotropic model is significantly less stiff). Nevertheless, since no experimental observations for such loading is available, it is impossible to assess at this time which of the two models better represents the reality.

The scant quantitative studies that identify the difference in the mechanical response when isotropic viz. orthotropic materials are considered, seem to suggest that the difference is negligible [13,17]. This conclusion, in view of our results herein, seems to be restricted to simplified loading conditions and not accurate for all regions of interest. Since the anisotropy is more pronounced in the femoral neck region this area is more sensitive to the different material assignment strategy. Similar conclusions (showing a difference in the mechanical response if isotropic or orthotropic materials were applied) were obtained in a recent work on a different organ (the mandible) [31]. In an ongoing research on *p*-FE predictions of failure initiation in the femur, a considerable difference is noticed between failure loads predicted by the isotropic and orthotropic models [49].

Several limitations of the present work have to be discussed. (a) Only four cadaver proximal femurs were investigated. (b) Only simple loading conditions were considered for the validation process. (c) The orthotropic MM model is based on a clinical CT scan and does not accurately represent the trabecular bone morphology. (d) The differences between the isotropic model and the orthotropic MM model are in the range of the experimental errors so unequivocal conclusions cannot be drawn regarding which model is better. Both models seem to provide very good correlation to experimental observations under the simplified loading condition.

To conclude, this study demonstrates the ability to apply *p*-FE technology to analyze patient-specific femurs with inhomogeneous micromechanics-based orthotropic material properties with material trajectories along the principal strains. The methods were numerically verified and validated by experimental observations. Future in vitro experiments resulting in a more complex state of stresses in the femur (a more realistic physiological load) is planned to further corroborate our conclusions. In this future study we will examine if indeed the inhomogeneous orthotropic material properties are necessary (as opposed to a simplified isotropic assumption) for a reliable simulation of the mechanical response, especially in the head and neck locations of the proximal femur. This is of major importance to failure analysis of osteoporotic bones, and the possibility to predict such failures as a function of bones' density and local geometry. We also intend to investigate "more physiological" loadings that may have a large influence on femur's mechanical response [45] by considering *p*-FE models loaded according to Refs. [47,50,51] and results compared to ex vivo experiments.

Acknowledgment

The authors thank Professor Charles Milgrom of the Hadassah Hospital in Jerusalem, for his help with the femurs' supply and CT scans and Professor Christian Hellmich of the Technical University of Vienna for assistance with the micromechanical models. The authors gratefully acknowledge the generous support of the Technical University of Munich–Institute for Advanced Study, funded by the German Excellence Initiative. Neither author has a conflict of interest to declare that could bias the presented work.

Appendix A: Micromechanics-Based Inhomogeneous Orthotropic Material Properties

Several of the micromechanics-based relations required for the computation of $\mathbb{C}_{\text{eff}}$ are provided herein following Refs. [26,31]. The orthotropic material tensor $\mathbb{C}_{\text{eff}}$ is represented in matrix notation, by replacing the subscripts *ij* (or *kl*) by *m* (or *n*) using the Voigt notation:

ij (or *kl*)	11	22	33	23 or 32	31 or 13	21 or 12
m (or *n*)	1	2	3	4	5	6

$$\mathbb{C}^{\text{exp}}_{\text{BM}} = \begin{pmatrix} C_{1111} & C_{1122} & C_{1133} & 0 & 0 & 0 \\ C_{1122} & C_{2222} & C_{2233} & 0 & 0 & 0 \\ C_{1133} & C_{2233} & C_{3333} & 0 & 0 & 0 \\ 0 & 0 & 0 & 2C_{2323} & 0 & 0 \\ 0 & 0 & 0 & 0 & 2C_{1313} & 0 \\ 0 & 0 & 0 & 0 & 0 & 2C_{1212} \end{pmatrix} \quad \text{(A1)}$$

and the following relations hold:

$$\mathbb{C}_{\text{H}_2\text{O}} = 3 \cdot k_{\text{H}_2\text{O}} \mathbb{J} \text{ where } J_{ijkl} = \frac{1}{3}\delta_{ij}\delta_{kl} \text{ and } k_{\text{H}_2\text{O}} = 2.3(\text{GPa}) \quad \text{(A2)}$$

$$I_{ijkl} = (\delta_{ik}\delta_{jl} + \delta_{il}\delta_{jk})/2 \quad \text{(A3)}$$

$$\mathbb{P}_{\text{cyl}} = \frac{1}{2\pi}\int_0^{2\pi} \mathbb{B} d\Phi \quad \text{(A4)}$$

$$B_{ijkl} = \frac{1}{4}(\xi_i \bar{G}_{jk}\xi_l + \xi_j \bar{G}_{ik}\xi_l + \xi_i \bar{G}_{jl}\xi_k + \xi_j \bar{G}_{il}\xi_k) \quad \text{(A5)}$$

$$\boldsymbol{G} = \boldsymbol{K}^{-1} \quad \text{(A6)}$$

$$\boldsymbol{K} = \xi \cdot \mathbb{C}_{\text{BM}} \cdot \xi, \quad \boldsymbol{K}_{jk} = \xi_i C_{\text{BM},ijkl}\xi_l \quad \text{(A7)}$$

$$\xi = \cos\Phi \hat{\boldsymbol{e}}_1 + \sin\Phi \hat{\boldsymbol{e}}_2 + \hat{\boldsymbol{e}}_3 \quad \text{(A8)}$$

where center dots denote the first-order tensor contraction (also called inner product).

The compliance matrix $\mathbb{S} = \mathbb{C}^{-1}$ for orthotropic materials presented in Eq. (A9) may be represented by the nine material constants $(E_1, E_2, E_3, G_{12}, G_{13}, G_{23}, \nu_{12}, \nu_{13}, \nu_{23})$, where 1 refers to the radial, 2 refers to the circumferential, and 3 refers to the longitudinal (axial) direction of the bone material:

$$\mathbb{S} = \begin{pmatrix} \frac{1}{E_1} & \frac{-\nu_{21}}{E_2} & \frac{-\nu_{31}}{E_3} & 0 & 0 & 0 \\ \frac{-\nu_{12}}{E_1} & \frac{1}{E_2} & \frac{-\nu_{32}}{E_3} & 0 & 0 & 0 \\ \frac{-\nu_{13}}{E_1} & \frac{-\nu_{23}}{E_2} & \frac{1}{E_3} & 0 & 0 & 0 \\ 0 & 0 & 0 & \frac{1}{G_{23}} & 0 & 0 \\ 0 & 0 & 0 & 0 & \frac{1}{G_{31}} & 0 \\ 0 & 0 & 0 & 0 & 0 & \frac{1}{G_{12}} \end{pmatrix} \quad \text{(A9)}$$

Bone matrix coefficients are computed by the nine orthotropic elastic properties see Ref. [52]. Six relevant studies are presented in Table 4 to provide an overview of the available current knowledge and to demonstrate the material properties range.

Table 4 Orthotropic elastic constant for bone matrix. Young's and Shear modulus are in GPa, SD = standard deviations, NR = not reported. 1: radial, 2: circumferential, and 3: longitudinal (axial) direction of the bone material.

Ref. year	Bone Site	Exp. method	No. of bones (specimen)	E_1^* (SD)	E_2 (SD)	E_3 (SD)	G_{12} (SD)	G_{13} (SD)	G_{23} (SD)	ν_{12} (SD)	ν_{13} (SD)	ν_{23} (SD)
[40]	femur	ultr.	5	12	13.4	20	4.53	5.61	6.23	0.235	0.371	0.376
1984			(60)	(1)	(1.1)	(1.5)	(0.3)	NR	NR	NR	NR	NR
[27][a]	femur	nano.	1	9.17	17.28	24.66	4.69	5.61	7.68	0.286	0.557	0.248
2009			(22)	(0.63)	(1.89)	(2.71)	(0.37)	(0.47)	(0.53)	(0.024)	(0.022)	(0.012)
[53]	tibia	ultr.	8	11.7	12.2	20.7	4.1	5.17	5.7	0.23	0.417	0.42
1996			(96)	(1.3)	(1.4)	(1.9)	(0.5)	(0.6)	(0.5)	(0.035)	(0.048)	(0.074)
[54]	tibia	nano.	1	16.6	17	25.1	NR	NR	NR	NR	NR	NR
2002			(12)	(1.5)	(2.2)	(2.1)						
[55]	femur	nano.	9	NR	NR	21.8	NR	NR	NR	NR	NR	NR
2002			NR			(2.1)						
[56]		MM	–	16.4	18.7	22.8	7.2	7.1	8.4	0.25	0.33	0.33
2008		based										

[a]In this case 1,2,3 represent the osteon level radial, circumferential and longitudinal directions.

Appendix B: Empirical Relations for Inhomogeneous Orthotropic Material Properties

AQ4 This appendix presents the MM-based properties compared to orthotropic material properties based on empirical correlation with density provided in Refs. [20,21]:

$$E_{1/2}^{\text{Cort}} = 2314 \cdot \rho_{\text{app}}^{1.57}(\text{MPa}) \quad \text{(B1)}$$

$$E_{3}^{\text{Cort}} = 2065 \cdot \rho_{\text{app}}^{3.09}(\text{MPa}) \quad \text{(B2)}$$

$$E_{1/2}^{\text{Trab}} = 1157 \cdot \rho_{\text{app}}^{1.78}(\text{MPa}) \quad \text{(B3)}$$

$$E_{3}^{\text{Trab}} = 1904 \cdot \rho_{\text{app}}^{1.64}(\text{MPa}) \quad \text{(B4)}$$

$$\nu_{ij} = \text{const} \quad \text{(B5)}$$

$$G_{ij} = \frac{G_{ij}^{\max} \cdot \rho_{\text{app}}^2}{\rho_{\max}^2}(\text{MPa}) \quad \text{(B6)}$$

$^*\rho_{\max}$ is the maximum apparent density and ρ_{app} is the apparent density as measured by QCT according to Ref. [57]. Here 1 denotes radial (medial-lateral in original manuscripts), 2 circumferential (anterior-posterior), and 3 the axial (superior-inferior) directions. These connections are denoted by the subscript "Wirtz" in the following.

Other empirical relations (for the cortical and trabecular bone) that correlate the Young's modulus to the density ρ are reported in Ref. [58]:

$$E_1^{\text{Cort}} = -6087 + 10 \cdot \rho(\text{MPa}) \quad \text{(B7)}$$

$$E_2^{\text{Cort}} = -4007 + 9 \cdot \rho(\text{MPa}) \quad \text{(B8)}$$

$$E_3^{\text{Cort}} = -6142 + 14 \cdot \rho(\text{MPa}) \quad \text{(B9)}$$

$$E_1^{\text{Trab}} = 0.004 \cdot \rho^{2.01}(\text{MPa}) \quad \text{(B10)}$$

$$E_2^{\text{Trab}} = 0.01 \cdot \rho^{1.88}(\text{MPa}) \quad \text{(B11)}$$

$$E_3^{\text{Trab}} = 0.58 \cdot \rho^{1.3}(\text{MPa}) \quad \text{(B12)}$$

$$\nu_{ij} = \text{const} \quad \text{(B13)}$$

$$G_{ij} = f(E_i, E_j, \nu_{ij})(\text{MPa}) \quad \text{(B14)}$$

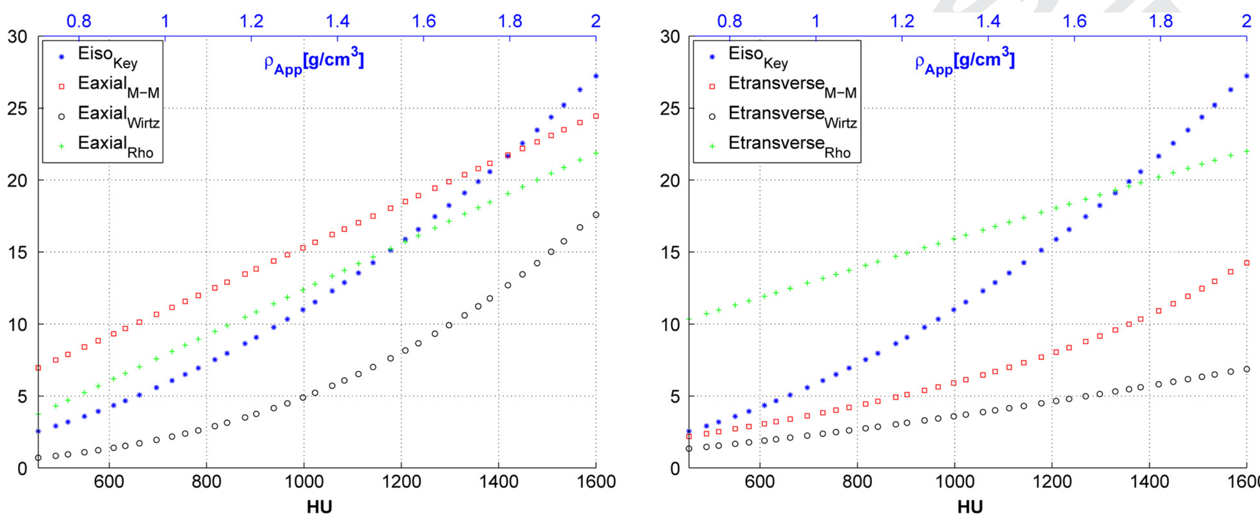

(a) Longitudinal direction (b) Transversal direction

Fig. 8 Young's modulus in different directions versus HU or apparent density for cortical bone. $E\text{iso}_{\text{Key}}$ ***represents the isotropic Young's modulus in Ref.*** **[36],** $E\text{axial}_{\text{MM}}$ **and** $E\text{transverse}_{\text{MM}}$ **are the axial and the transversal Young's modulus computed by the micro-mechanics model,** $E\text{axial}_{\text{Wirtz}}$ ***and*** $E\text{transverse}_{\text{Wirtz}}$ **are the axial and transversal Young's modulus according to Eqs. (B2) and (B1), and** $E\text{axial}_{\text{Rho}}$ ***and*** $E\text{transeverse}_{\text{Rho}}$ **is the axial and transversal Young's modulus according to Eqs. (B9) and (B7).**

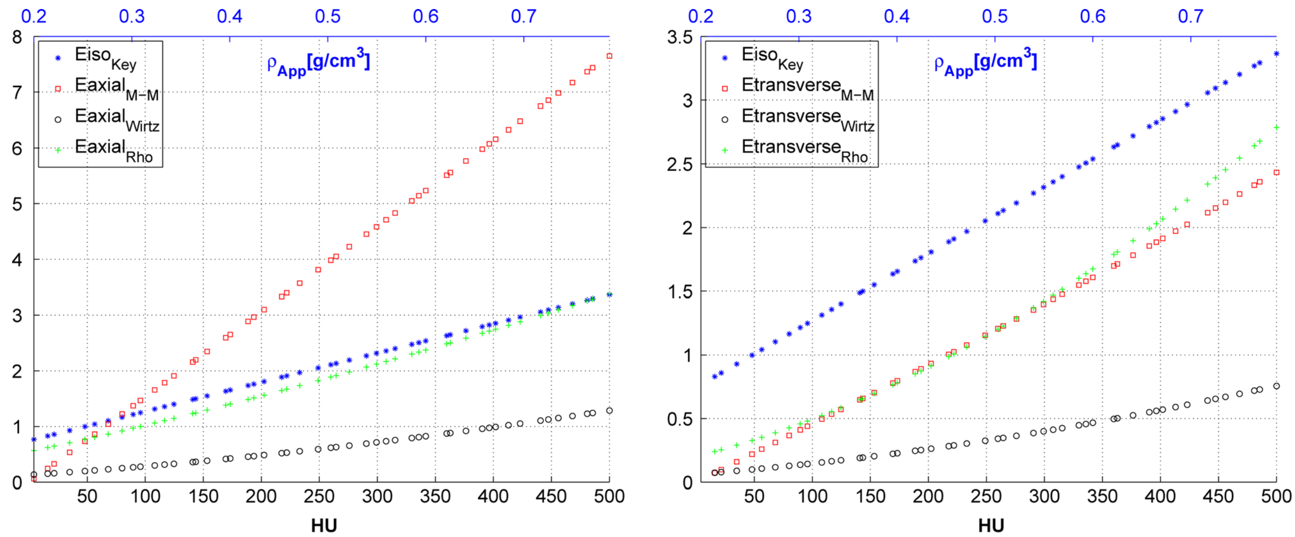

(*a*) Longitudinal direction (*b*) Transversal direction

Fig. 9 Young's modulus in different directions versus HU or apparent density for trabecular bone

These connections are denoted by the subscript "Rho" in the following. In Rho the density of cortical bone was determined by Archimedes' law and for the trabecular bone by wet weight divided by volume of the specimens. Poisson ratios are assumed to be constant and the shear moduli are calculated as a function of Poisson ratio and Young's modulus.

Comparison of the Material Properties Determined by the Different Methods. Because Young's modulus has the most significant influence on the bone mechanical response, we herein illustrate the variation between the different orthotropic relations. The mathematical relationships of Young's modulus in different directions (longitudinal and transversal) as a function of HU or apparent density and the values obtained using MM methods are presented in Figs. 8 and 9 for cortical and trabecular regions, respectively. The Young's modulus from the isotropic model [36] is also presented. The density is taken as the apparent density computed as a linear relation to HU (for comparison only).

To conclude, well-known elasticity-density relationships for orthotropic materials were selected and normalized according to bone density and HU. The results show that the values extracted using micromechanics (MM) methods are in the range of the selected relations more close to the elasticity-density relationships suggested by Ref. [58]. The elasticity-density relationships suggested by Wirtz et al. [20] and used in many studies to investigate the influence of anisotropic in FE models yield significantly lower values in Young's modulus. The variability in the material values was expected, as already noticed for isotropic elasticity-density relationships.

References

[1] Keyak, J. H., Meagher, J. M., Skinner, H. B., and Mote, J. C. D., 1990, "Automated Three-Dimensional Finite Element Modelling of Bone: A New Method," ASME J. Biomech. Eng., **12**, pp. 389–397.
[2] Martelli, S., Taddei, F., Varini, E., Cristofolini, L., Gill, H. S., and Viceconti, M.,. 2005, "Accuracy of Subject Specific Finite-Element Models of Long Bones From CT Data: An in-vitro Study," *Proceedings of ICCB II*, Vol. **1**, pp. 251–265.
[3] Yosibash, Z., Trabelsi, N., and Milgrom, C., 2007, "Reliable Simulations of the Human Proximal Femur by High-Order Finite Element Analysis Validated by Experimental Observations," J. Biomech., **40**, pp. 3688–3699.
[4] Trabelsi, N., Yosibash, Z., and Milgrom, C., 2009, "Validation of Subject-Specific Automated p-FE Analysis of the Proximal Femur," J. Biomech., **42**, pp. 234–241.
[5] Helgason, B., Taddei, F., Palsson, F., Schileo, E., Cristofolini, L., Viceconti, M., and Brynjolfsson, S., 2008, "A Modified Method for Assigning Material Properties to FE Models of Bones," Med. Eng. Phys., **30**, pp. 444–453.
[6] Liao, S. H., Tong, R. F., and Dong, J. X., 2007, "Anisotropic Finite Element Modeling for Patient-Specific Mandible," J. Comput. Meth. Prog. Biomed., **88**(3), pp. 197–209.
[7] Taddei, F., Schileo, E., Helgason, B., Cristofolini, L., and Viceconti, M., 2007, "The Material Mapping Strategy Influences the Accuracy of CT-based Finite Element Models of Bones: An Evaluation Against Experimental Measurements," Med. Eng. Phys., **29**(9), pp. 973–979.
[8] Viceconti, M., Bellingeri, L., Cristofolini, L., and Toni, A., 1998, "A Comparative Study on Different Methods of Automatic Mesh Generation of Human Femurs," Med. Eng. Phys., **20**, pp. 1–10.
[9] Viceconti, M., Davinelli, M., Taddei, F., and Cappello, A., 2004, "Automatic Generation of Accurate Subject-Specific Bone Finite Element Models to be Used in Clinical Studies," J. Biomech., **37**, pp. 1597–1605.
[10] Yosibash, Z., Padan, R., Joscowicz, L., and Milgrom, C., 2007, "A CT-Based High-Order Finite Element Analysis of the Human Proximal Femur Compared to in-vitro Experiments," ASME J. Biomech. Eng., **129**(3), pp. 297–309.
[11] Pitto, T. P., Mueller, L. A., Reilly, K., and Munro, C. J., 2007, "The Use of Sparse CT Datasets for Auto-Generating Accurate FE Models of the Femur and Pelvis," J. Biomech., **40**, pp. 26–35.
[12] Keyak, J., and Skinner, H., "Three-Dimensional Finite Element Modelling of Bone: Effect of Element Size," ASME J. Biomech. Eng., **14**, pp. 483–489.
[13] Peng, L., Bai, J., Zeng, Z., and Zhou, Y., 2006, "Comparison of Isotropic and Orthotropic Material Property Assignments on Femoral Finite Element Models Under Two Loading Conditions," Med. Eng. Phys., **28**, pp. 227–233.
[14] Schileo, E., Taddei, F., Malandrino, A., Cristofolini, L., and Viceconti, M., 2007, "Subject-Specific Finite Element Models can Accurately Predict Strain Levels in Long Bones," J. Biomech., **40**, pp. 2982–2989.
[15] Schileo, E., DallAra, E., Taddei, F., Malandrino, A., Schotkamp, T., Baleani, M., and Viceconti, M., 2008, "An Accurate Estimation of Bone Density Improves the Accuracy of Subject-Specific Finite Element Models," J. Biomech., **41**, pp. 2483–2491.
[16] Duchemin, L., Boussonb, V., Raossanaly, C., Bergot, C., Laredob, J. D., Skalli, W., Mitton, D., 2008, "Prediction of Mechanical Properties of Cortical Bone by Quantitative Computed Tomography," Med. Eng. Phys., **30**, pp. 321–328.
[17] Baca, V., Horak, Z., Mikulenka, P., and Dzupa, V., 2008, "Comparison of an Inhomogeneous Orthotropic and Isotropic Material Models Used for FE Analyses," J. Med. Eng. Phys., **30**, pp. 924–930.
[18] Yang, H., Ma, X., Guo, T., 2010, "Some Factors That Affect the Comparison Between Isotropic and Orthotropic Inhomogeneous Finite Element Material Models of Femur," Med. Eng. Phys., **32**, pp. 553–560.
[19] Lotz, J. C., Gerhart, T. N., and Hayes, W. C., 1991, "Mechanical Properties of Metaphyseal Bone in the Proximal Femur," J. Biomech., **24**, pp. 317–329.
[20] Wirtz, D., Schiffers, N., Pandorf, T., Radermacher, K., Weichert, D., and Forst, R., 2000, "Critical Evaluation of Known Bone Material Properties to Realize Anisotropic FE-Simulation of the Proximal Femur," J. Biomech., **33**, pp. 1325–1330.
[21] Taylor, W. R., Roland, E., Ploeg, H., Hertig, D., Klabunde, R., Warner, M. D., Hobatho, M. C., Rakotomanana, L., and Clift, S. E., 2002, "Determination of Orthotropic Bone Elastic Constants Using FEA and Modal Analysis," J. Biomech., **35**, pp. 767–773.
[22] Wirtz, D. C., Pandorf, T., Portheine, F., Radermacher, K., Schiffers, N., Prescher, A., Weichert, D., and Fritz, U. N., 2003, "Concept and Development of

an Orthotropic FE Model of the Proximal Femur," J. Biomech., **36**, pp. 289–293.

[23] Shahar, R., Zaslansky, P., Barak, M., Friesem, A., Currey, J., and Weiner, S., 2007, "Anisotropic Poisson's Ratio and Compression Modulus of Cortical Bone Determined by Speckle Interferometry," J. Biomech., **40**, pp. 252–264.

[24] Tabor, Z., and Rokita, E., 2007, "Quantifying Anisotropy of Trabecular Bone From Gray-Level Images," Bone, **40**, pp. 966–972.

[25] Schneider, R., Faust, G., Hindenlang, U., Helwig, P., 2009, "Inhomogeneous, Orthotropic Material Model for the Cortical Structure of Long Bones Modelled on the Basis of Clinical CT or Density Data," Comput. Meth. Appl. Mech. Eng., **198**, pp. 2167–2174.

[26] Fritsch, A., and Hellmich, C., 2007, "Universal Microstructural Patterns in Cortical and Trabecular, Extracellular and Extravascular Bone Materials: Micromechanics-Based Prediction of Anisotropic Elasticity," J. Theor. Biol., **244**, pp. 597–620.

[27] Franzoso, G., and Zysset, P., 2009, "Elastic Anisotropy of Human Cortical Bone Secondary Osteons Measured by Nanoindentation," ASME J. Biomech. Eng., ■, pp. 021001/1–021001/11.

[28] Cowin, S., 1985, "The Relationship Between the Elasticity Tensor and the Fabric Tensor," Mech. Mater., **4**, 137–147.

[29] Ogdgaard, A., 1997, "Three-Dimensional Methods for Quantification of Cancellous Bone Architecture," Bone, **20**(4), pp. 315–328.

[30] Chevalier, Y., Pahr, D., and Zysset, P., 2009, "The Role of Cortical Shell and Trabecular Fabric in Finite Element Analysis of the Human Vertebral Body," J. Biomech. Eng., **13**, pp. 111003–1–111003-12.

[31] Hellmich, C., Kober, C., and Erdmann, B., 2008, "Micromechanics-Based Conversion of CT Data Into Anisotropic Elasticity Tensors, Applied to FE Simulations of a Mandible," Ann. Biomed. Eng., **36**, pp. 108–122.

[32] Yosibash, Z., Trabelsi, N., and Hellmich, C., 2008, "Subject-Specific p-FE Analysis of the Proximal Femur Utilizing Micromechanics Based Material Properties," Int. J. Multiscale Comput. Eng., **6**(5), pp. 483–498.

[33] Szabó, B. A., and Babuîska, I., 1991, *Finite Element Analysis* (John-Wiley, New York).

[34] Carter, D., and Hayes, W., 1977, "The Compressive Behavior of Bone as a Two-Phase Porous Structure," J. Bone Joint Surg. Am., **59**, pp. 954–962.

[35] Cody, D. D., Hou, F. J., Divine, G. W., and Fyhrie, D. P., 2000, "Short Term in vivo Study of Proximal Femoral Finite Element Modeling," Ann. Biomed. Eng., **28**, pp. 408–414.

[36] Keyak, J., and Falkinstein, Y., 2003, "Comparison of in situ and in vitro CT Scan-Based Finite Element Model Predictions of Proximal Femoral Fracture Load," Med. Eng. Phys., **25**, pp. 781–787.

[37] Keller, T. S., 1994, "Predicting the Compressive Mechanical Behavior of Bone," J. Biomech., **27**, pp. 1159–1168.

[38] Morgan, E. F., Bayraktar, H. H., and Keaveny, T. M., 2003, "Trabecular Bone Modulus-Density Relationships Depend on Anatomic Site," J. Biomech., **36**, pp. 897–904.

[39] Zaoui, A., 2002, "Continuum Micromechanics: Survey," J. Eng. Mech. (ASCE), **128**(8), pp. 808–816.

[40] Ashman, R. B., Cowin, S. C., van Buskirk, W. C., and Rice, J. C., 1984, "A Continuous Wave Technique for the Measurement of the Elastic Properties of Cortical Bone," J. Biomech., **17**(5), pp. 349–361.

[41] Kober, C., Erdmann, B., Hellmich, C., Sader, R., and Zeilhofer, H.-F., 2006, "Consideration of Anisotropic Elasticity Minimizes Volumetric Rather Than Shear Deformation in Human Mandible," Comput. Meth. Biomech. Biomed. Eng., **9**(2), pp. 91–101.

[42] Pietruszczak, S., Inglis, D., and Pande, G., 1999, "A Fabric-Dependent Fracture Criterion for Bone," J. Biomech., **32**(10), pp. 1071–1079.

[43] Wolff, J., 1986, *The Law of Bone Remodeling* (Springer, Berlin) (translation of the German 1892 edition).

[44] Hert, J., Fiala, P., and Petrtyl, M., 1994, "Osteon Orientation of the Diaphysis of the Long Bones in Man," Bone, **15**(3), pp. 269–277.

[45] Cristofolini, L., Juszczyk, M., Taddei, F., and Viceconti, M., 2009, "Strain Distribution in the Proximal Human Femoral Metaphysis," Proc. Inst. Mech. Eng., Part H: J. Eng. Med., **223**, pp. 273–288.

[46] Sokolnikoff, I. S., 1956, *Mathematical Theory of Elasticity* (McGraw-Hill, New York).

[47] Bergmann, G., Deuretzbacher, G., Heller, M. O., Graichenm, F., Rohlmann, A., Strauss, J., Haas, N. P., and Duda, G., 2001, "Hip Contact Forces and Gait Patterns From Routine Activities," J. Biomech., **34**, pp. 859–871.

[48] Ohman, C., Baleani, M., Perilli, E., DallAra, E., Tassani, S., Baruffaldi, F., and Viceconti, M., 2007, "Mechanical Testing of Cancellous Bone From the Femoral Head: Experimental Errors Due to Off-Axis Measurements," J. Biomech., **40**, pp. 2426–2433.

[49] Yosibash, Z., Tal, D., and Trabelsi, N., 2010, "Predicting the Yield of the Proximal Femur Using High Order Finite Element Analysis With Inhomogeneous Orthotropic Material Properties," Philos. Trans. R. Soc. London, Ser. A, **368**, pp. 2707–2723.

[50] Heller, M. O., Bergmann, G., Deuretzbacher, G., Durselen, L., Pohl, M., Claes, L., and Haas, N. P., 2001, "Musculo-Skeletal Loading Conditions at the Hip During Walking and Stair Climbing," J. Biomech., **34**, pp. 883–893.

[51] Heller, M. O., Bergmann, G., Kassi, J.-P., Claes, L., and Haas, N. P., 2005, "Determination of Muscle Loading at the Hip Joint for Use in Pre-Clinical Testing," J. Biomech., **38**, pp. 1155–1163.

[52] Ting, T. C. T., 1996, *Anisotropic Elasticity Theory and Applications* (Oxford Engineering Science Series, Oxford).

[53] Rho, J., 1996, "An Ultrasonic Method for Measuring the Elastic Properties of Human Tibial Cortical and Cancellous Bone," J. Ultrasonics, **34**(8), pp. 777–778.

[54] Fan, Z., Swadener, J., Rho, J., Roy, M., and Pharr, G., 2002, "Anisotropic Properties of Human Tibial Cortical Bone as Measured by Nanoindentation," J. Orthop. Res., **20**(4), pp. 806–810.

[55] Rho, J., Zioupos, P., Currey, J., and Pharr, G., 2002, "Microstructural Elasticity and Regional Heterogeneity in Human Femoral Bone of Various Ages Examined by Nano-Indentation," J. Biomech., **35**(2), pp. 189–198.

[56] Yoon, Y., and Cowin, S., 2008, "The Estimated Elastic Constants for a Single Bone Osteonal Lamella," J. Biomech. Model. Mechanobiol., **7**, pp. 1–11.

[57] Lotz, J. C., Gerhart, T. N., and Hayes, W. C., 1990, "Mechanical Properties of Trabecular Bone From the Proximal Femur: A Quantitative CT Study," J. Comput. Assisted Tomography, **14**(1), pp. 107–114.

[58] Rho, J. Y., Hobatho, M. C., and Ashman, R. B., 1995, "Relations of Mechanical Properties to Density and CT Numbers in Human Bone," Med. Eng. Phys., **17**, pp. 347–355.

AQ1: Author, please note that references must be cited in numerical order and check renumbering throughout carefully.

AQ2: Author, please check renumbering of equations and citations in Appendix B.

AQ3: Author, please supply volume for Ref. 27.

AQ4: Author, please check authors for Refs. 50,51,11.